

Tidal Dynamics in the Ross Sea

ROBIN ROBERTSON*, AIKE BECKMANN, and HARTMUT HELLMER
Alfred-Wegener-Institut für Polar- und Meeresforschung
Postfach 12 0161
D-27515 Bremerhaven
Germany

*corresponding author
now at
Lamont-Doherty Earth Observatory
Columbia University
Palisades, New York 10964

Phone numbers and email:
Robin Robertson: (845) 365- 8527
(fax) (845) 365- 8157
rroberts@ldeo.columbia.edu
Aike Beckmann: : 49 (0) 471 4831-1793
(fax) 49 (0) 471 4831-1797
beckmann@ awi-bremerhaven.de
Hartmut Hellmer: 49 (0) 471 4831-1794
(fax) 49 (0) 471 4831-1797
hellmer@ awi-bremerhaven.de

1) Karen - Gouretski ref

for submission to special issue of Antarctic Science (Ross Sea)
December 28, 2001

Abstract

In certain regions of the Southern Ocean, tidal energy is believed to foster the mixing of different water masses, which eventually contribute to the formation of deep and bottom waters. The Ross Sea is one of the major ventilation sites of the global ocean abyss and a region of sparse tidal observations. We investigated tidal dynamics in the Ross Sea using a three-dimensional sigma coordinate model, the Regional Ocean Model Systems (ROMS). Realistic topography and hydrography from existing observational data were used with a single tidal constituent, the semi-diurnal M_2 . The model fields faithfully reproduced the major features of the tidal circulation and had reasonable agreement with ten existing tidal elevation observations and forty-two existing tidal current measurements. The differences were attributed primarily to topographic errors.

Internal tides were generated at the continental shelf/slope break and other areas of steep topography. Strong vertical shears in the horizontal velocities occurred under and at the edges of the Ross Ice Shelf and along the continental shelf/slope break. Estimates of lead formation based on divergence of baroclinic velocities were significantly higher than those based on barotropic velocities, reaching over 10% at the continental shelf/slope break.

Key Words: Tides, Ross Sea, Internal tides

1. Introduction

Barotropic and baroclinic tides play significant roles in ocean mixing [Munk and Wunsch, 1998; Muench et al., 2002] and in the ocean-atmosphere heat transfer [Padman and Kottmeier, 2000; Robertson, 2001b]. Barotropic tides increase benthic mixing through higher benthic shear and baroclinic tides increase mid-water column mixing through shear instabilities. In the Antarctic seas, mixing along the continental slope can affect formation of deep and bottom waters and their ventilation. In addition, mixing has the potential to affect the heat transport from the Warm Deep Water to the surface ice and influence the ice cover [McPhee et al., 1996; Muench et al., 2002; Beckmann et al., 2001]. As early as the 1800's, it was recognized that tides induce lead formation in the ice due to convergence and divergence of the velocities [Nansen, 1898]. The lead formation then affects the ocean-atmosphere heat transfer. Thus, through multiple mechanisms, tides have the capability to influence mixing and heat transfer in the Ross Sea. In order to understand and quantify their mixing contribution, the tidal dynamics must first be understood.

Tidal observations for the Ross Sea are rather sparse (dots and triangles in Figure 1), so models have been used to fill in gaps in the data and provide estimates of the tidal dynamics. The barotropic tides in the Ross Sea have been modeled by MacAyeal [1984] and Padman [personal communication]. However, the vertical structure has not been addressed. Our goal was to investigate the three-dimensional M_2 tidal dynamics in the Ross Sea using the Regional Ocean Modeling System (ROMS), which is described in Section 2. Section 3 gives the model results and compares them to the existing observations. Implications of the model results are discussed in Section 4.

2. Model Description

2.1 Model

Terrain-following models, such as the Princeton Ocean Model (POM) and ROMS, are preferable for simulating regions with widely varying topography, such as the Ross Sea, due to

their more realistic representations of the topography and benthic boundary layer using fewer vertical levels than z-level models. Both POM and ROMS have been used for modeling internal tides [POM: *Holloway, 1996; Robertson, 2001a*; ROMS: *Hetland, personal communication*]. A comparison of the performance of POM and ROMS for a region in the Weddell Sea, indicated that ROMS was preferable for modeling internal tides in a weakly stratified ocean [*Robertson et al., 2002*].

Several different numerical options to simulate the different physical processes are available in ROMS. In these simulations, third order upstream differencing for horizontal advection, Laplacian lateral diffusion along sigma surfaces ($10 \text{ m}^2 \text{ s}^{-1}$), and the *Large-McWilliams-Doney* vertical mixing scheme were used. *Flather* radiative boundary conditions were implemented for the barotropic mode velocities and flow relaxation boundary conditions for the baroclinic mode velocities and tracers. Tidal forcing was implemented by setting elevations along all the open boundaries, with the coefficients taken from a two-dimensional model of the region [*Padman, personal communication*]. Only one tidal constituent, the semi-diurnal M_2 , was used. The barotropic and baroclinic mode time steps were 8 s and 240 s, respectively, and the simulations were run for 17 days, with hourly data from the last 2 days used for analysis.

2.2 Topography and Hydrography

For the Ross Sea, ROMS was modified to include the presence of an ice shelf. The ice shelf was assumed to be floating. Both mechanical and thermodynamic effects were included following *Robertson* [1999; 2001a] and *Hellmer and Olbers* [1989], respectively.

The model domain (Figure 1) covered the Ross Sea with a spacing of 0.045° in latitude, 0.186° in longitude, and 24 vertical levels. North of 78°S , the water column thickness, the distance between the bottom and the ocean surface (or ice shelf base), was taken from *Smith and Sandwell* [1997]. South of 78°S and under the ice shelf, the water column thickness and ice shelf thickness were supplied by *Greischar et al.* [1992 (electronic version supplied by *Greischar*)]. Neither, the water column nor the ice shelf thicknesses were smoothed. The minimum water

column thickness was set to 50 m, which entailed artificially deepening portions of the region under the ice shelf, particularly near the eastern grounding line.

Initial potential temperature, θ , and salinity, S , fields were assembled from the World Ocean Circulation Experiment (WOCE) Hydrographic Programme Special Analysis Center [Gouretski et al., 1999], except under the ice shelf. Here, the hydrography was essentially a four layer system based on a θ and S profile through the ice shelf at a single location (J9 [Jacobs, 1989]). The uppermost layer was 40 m thick with θ = the freezing point of water at the depth of the ice shelf base and S = 34.39 psu. The second layer was 100 m thick with θ = 0.06°C above the freezing point of water for the depth. θ increased linearly between this value and that of the lowermost layer within the 50 m thick third layer. The lowermost layer encompassed the remaining water column (deeper than 190 m below the ice shelf base) with a θ = -1.87°C and a S = 34.83 psu. S increased linearly between values in the uppermost and the lowermost layers over the 150 m of the middle two layers.

2.3 Model Outputs

Elevation, η , and depth-independent velocities, U_2 and V_2 , are produced by the two-dimensional (barotropic) mode of the model and θ , S , and depth-dependent velocities, U_3 , V_3 , and W_3 , by the three-dimensional (baroclinic) mode. Foreman's tidal analysis routines were used to analyze these fields [Foreman 1977; 1978].

3. Results

3.1 Elevations and Depth-Independent Velocities

The predominant feature of the M_2 tidal elevation amplitude was the amphidromic point located at $\sim 178^\circ$ W, 82° S (Figure 2). This amphidromic point results from interference between the positive and negative phases of the semidiurnal tide and is dependent on the relative size of the Ross Basin and the tidal wavelength [MacAyeal, 1984]. The M_2 tidal elevation amplitudes in

the Ross Sea were generally small, ≤ 5 cm, although values > 10 cm were reached under the ice shelf, particularly the eastern portion, and along the western margin, north of Ross Island.

To evaluate the performance of the model, the modeled elevation amplitudes and phases were compared to those of the existing observations (Table 1), whose locations are shown as dots in Figure 1. The model elevation amplitudes were generally higher than the observation by 2-4 cm s^{-1} with seven of the ten values exceeding the observational uncertainty, 2 cm [Williams and Robinson, 1980] (Table 1). The largest discrepancy, 10 cm, occurred at the southern grounding line. The phases did not agree as well, with only half of the points agreeing within 45° (Table 1). The phase changes rapidly in the vicinity of the amphidromic point and even a small error in the location of this point results in significant errors in the phases.

For two major reasons, most of the differences between the observations and the model estimates are believed to be a result of topographic errors. First, the bathymetry and ice shelf thickness under the Ross Ice Shelf are not well known and the model results are quite sensitive to errors in their estimates. Second, the artificial increase in the water column thickness reduced the bottom friction and dissipated less of the tidal energy, particularly at the back of the ice shelf. This not only had the effect of increasing the elevation, but also the group speed of the tidal Kelvin wave, consequently modifying the location of the amphidromic point. This effect has been previously seen in model results [MacAyeal, 1984; Robertson et al., 1998; Padman et al., 1999]. The incorrect position of the amphidromic point location accounted for much of the discrepancy between the observations and the model results, particularly for the phases.

The model estimates were also compared to the results of two different two-dimensional tidal models, [MacAyeal, 1984; Padman, personal communication]. Padman's model (grid spacing: ~ 6 km in longitude and ~ 9 km in latitude) performed similarly to ROMS; however, MacAyeal's model (grid spacing: ~ 10 km in longitude and ~ 10 km in latitude) showed slightly less agreement. ROMS had significantly better phase agreement than the other two models (Table 1). Both of these models also suffer from topographic errors.

The largest major axes of the tidal ellipses for the depth-independent velocities occurred in the southwest corner of the ice shelf cavity (Figure 3). Elsewhere, the major axes were generally quite small, less than 4 cm s^{-1} . The velocities increased along the continental slope and high values occurred over the Iselin Bank. Again the topography was the primary controlling factor for the depth-independent velocities, as has been previously noted for a two-dimensional tidal model [Robertson *et al.*, 1998].

In conclusion, the model reasonably simulated the major features of the observed barotropic tidal flow in the Ross Sea. The differences between the model estimates and the observations were primarily attributed to lack of detailed topographic data for the ice shelf cavity.

3.2 Depth-Dependent Response

To further evaluate the response of the model, the major axes of the tidal ellipses for depth-dependent velocities were compared to those of forty-two current meters on seventeen moorings, whose locations are shown as triangles in Figure 1. The model estimates for the major axes were generally larger than the observed values (Figure 4), but were within the observational uncertainty of 1.7 cm s^{-1} [Pillsbury and Jacobs, 1984] for twenty-eight of the forty-two sites. At two locations over Iselin Bank, the observations reported extremely high tidal benthic velocities (bottom values in Figures 4e and 4j), which were not seen in the model results. These may be locally high values and a result of small-scale topographic features unresolvable with the model topography. The higher values of the model estimates are again attributed to the lack of accurate, high resolution topographic data and the higher group wave speed resulting from the limit on the water column thickness.

The M_2 critical latitude, $78^\circ 28.8' \text{ S}$, crosses through the domain (Figure 1 and dashed line in Figure 5). At the critical latitude the inertial frequency equals the tidal frequency. This affects both the generation and propagation of internal tides. Linear internal wave theory predicts that internal waves will not be generated nor propagate poleward of the critical latitude. (A more

extensive explanation of the relevant linear internal wave theory is provided in *Robertson* [2001a].)

Generation and propagation of internal tides occurred over the continental slope and steep topography equatorward of the critical latitude (areas indicated with IT in Figures 5a-5d), especially in the western Ross Sea (Figures 5a-5c), where the continental slope is equatorward of critical latitude (Figure 1). In the eastern Ross Sea, east of 174° W, the continental slope is poleward of the critical latitude (Figure 1) and the generation of internal tides is reduced (areas marked RG in Figures 5d and 5e). The internal tides showed the expected wavelengths and propagated along the expected wave characteristics according to linear internal wave theory.

Strong vertical shears in the horizontal velocities are an indicator of potential mixing. They occurred under and at the front of the ice shelf (areas marked VS in Figures 5a-5f). Although the existence of internal tides is not expected in a continuously stratified fluid according to linear internal wave theory, it is quite possible for a baroclinic mode tide to exist in the multiple layer system [*Kundu*, 1990, p. 233], such as that of the initial hydrographic conditions in the ice cavity. A two layer response is apparent under the ice shelf with the upper two layers (140 m) essentially responding together as the top layer and the lowermost layer as the bottom layer (area marked 2L in Figure 5a). Additionally, strong vertical shears in the horizontal velocities occurred in the regions of internal tide generation (areas marked IT in Figures 5a-5e).

4. Implications of Model Results

Lead formation due to tidal divergence can affect the ocean-atmosphere heat flux. Since the heat flux increases by 1-2 orders of magnitude over leads compared to an ice covered ocean [*Maykut*, 1986], a lead formation percentage of 1-10 % would significantly increase the ocean-atmosphere heat flux. Lead formation percentages, $L_{\%}$ were estimated from the divergence of both the depth-independent velocities and the depth-dependent velocities at the surface according to

$$L_{\%} = 0.5T\langle\nabla\cdot\mathbf{V}\rangle \quad (1)$$

where T is the tidal period (34,712 s for M_2), $\nabla\cdot\mathbf{V}$ is the divergence of either the depth-independent velocities or the depth-dependent surface velocities (i.e., $\nabla\cdot\mathbf{V} = \partial U_2/\partial x + \partial V_2/\partial y$ or $= \partial U_3/\partial x + \partial V_3/\partial y$, respectively) and angle brackets indicate the standard deviation of the quantity. High lead formation percentages occurred over steep topographic changes along the continental shelf break (Figure 6). The estimate of lead formation increased by a factor of 2-5 for the depth-dependent surface velocities compared to the depth-independent velocities (Figures 6a and 6b). These crude estimates are likely to be an upper bound, since they do not include effects of the ice motion on the ocean dynamics or damping or blockage of the ice motion. Additionally, only one tidal constituent was used in these estimates and estimates using multiple constituents will be different due to constructive and destructive interference between the constituents. Despite the caveats, these rough estimates indicate that tides can significantly increase the ocean-atmosphere heat transfer.

Acknowledgements:

Thanks are due to E. Curchitser, H. Garcia, and A. Shchepetkin for assistance with ROMS and helpful discussions on inclusion of the ice shelf. (Thank reviewers when appropriate.) This study was funded by grant INT-0000394 from the National Science Foundation (NSF).

Additionally, the Alfred-Wegener-Institut für Polar- und Meeresforschung provided support for A. Beckmann and H. Hellmer and computer equipment and office space for R. Robertson. This is Lamont publication #####.

References

Beckmann, A., R. Timmermann, A. F. Pereira, V. Mohn, 2001, Sea ice anomalies in the eastern Weddell Sea, *CLIVAR Exchanges*, 6, 15-16.

- Foreman, M. G. G., 1977, *Manual for tidal height analysis and prediction*, Pacific Marine Science Report No. 77-10, Institute of Ocean Sciences, Patricia Bay, Sidney, B.C., 58 pp..
- Foreman, M. G. G., 1978, *Manual for tidal current analysis and prediction*, Pacific Marine Science Report No. 78-6, Institute of Ocean Sciences, Patricia Bay, Sidney, B.C., 70 pp..
- Gouretski, V. V., and K. Jancke, 1999, A Description and Quality Assessment of the Historical Hydrographic Data for the South Pacific Ocean. *Jour. of Atmos.and Oceanic Tech.*, 16, 1791-1815.
- Greischar, L. L., C. R. Bentley, and L. R. Whiting, 1992, An analysis of gravity measurements on the Ross Ice Shelf, Antarctica, in Contributions to Antarctic Research III (D. H. Elliot, ed.), Antarctic Research Series Vol. 57, American Geophysical Union, Washington D. C., 105-155.
- Hellmer, H. H., and D. J. Olbers, 1989, A two-dimensional model for the thermohaline circulation under an ice shelf, *Antarctic Science*, 4, 325-326.
- Holloway, P. E., 1996, A numerical model of internal tides with application to the Australian northwest shelf, *J. Phys. Oceanogr.*, 26, 21-37.
- Jacobs, S. S., 1989, Marine controls on modern sedimentation on the Antarctic continental shelf, *Mar. Geo.*, 85, 121-153.
- Kundu, P. K., 1990, *Fluid Mechanics*, Academic Press, Inc., San Diego, CA, 638 pp..
- MacAyeal, D. G., 1984, Numerical simulation of the Ross Sea tide, *J. Geophys. Res*, 89, 607-615.
- Maykut, G. H., 1986, The surface heat and mass balance, in *Geophysics of Sea Ice*, edited by N. Untersteiner, Plenum Press, NY, 395-463.
- McPhee, M. G., S. F. Ackley, P. Guest, B. A. Huber, D. G. Martinson, J. H. Morison, R. D. Muench, L. Padman, and T. P. Stanton, 1996, The Antrarctic Flux Zone Experiment, *Bull. American Met. Soc.*, 77, 1221-1232.
- Muench, R. D., L. Padman, S. L. Howard, and E. Fahrbach, 2001, Upper ocean diapycnal mixing in the northwestern Weddell Sea, accepted for a special issue of *Deep-Sea Res.*, 2002.

Munk, W. and C. Wunsch, 1998, The moon and mixing: abyssal recipes II, *Deep-Sea Res.*, 45, 1977-2010.

Nansen, F., 1898, *Farthest North*, vol. 1, George Newnes, London.

Padman, L., R. Robertson, and K Nicholls, 1999, Modeling tides in the southern Weddell Sea: updated model with new bathymetry from ROPEX, *Fichner-Ronne Ice Shelf Programme, Rep. 12*, 65-73.

Padman, L., and C. Kottmeier, 2000, High-frequency ice motion and divergence in the Weddell Sea, *J. Geophys. Res.*, 105, 3379-3400.

Pillsbury, R. D., and S. S. Jacobs, 1985, Preliminary observations from long-term current meter moorings near the Ross Ice Shelf, Antarctica, *Oceanology of the Antarctic Continental Shelf, Ant. Res. Ser.* 43, 87-107.

Robertson, R., 2001a, Internal tides and baroclinicity in the southern Weddell Sea: Part I: Model description, and comparison of model results to observations, *J. Geophys. Res.*, 106, 27001-27016.

Robertson, R., 2001b, Internal tides and baroclinicity in the southern Weddell Sea: Part II: Effects of the critical latitude and stratification, *J. Geophys. Res.*, 106, 27017-27034.

Robertson, R., 1999, Mixing and heat transport mechanisms for the upper water column in the Weddell Sea, Ph.D. Dissertation, College of Oceanic and Atmospheric Sciences, Oregon State University.

Robertson, R., A. Beckmann, and H. Hellmer, 2002, A comparison of POM and ROMS for modeling internal tides in weak stratification, in preparation.

Robertson, R., L. Padman, and G. D. Egbert, 1998, Tides in the Weddell Sea, in *Ocean, Ice, and Atmosphere: Interactions at the Antarctic Continental Margin*, Antarctic Research Series, 75, 341-369.

Smith, W. H. F., and D. T. Sandwell, 1997, Global seafloor topography from satellite altimetry and ship depth soundings, *Science*, 277, 1956-1962.

Robertson et al.: Tidal Dynamics in the Ross Sea

Williams, R. T., and E. S. Robinson, 1980, The ocean tide in the southern Ross Sea, *J. Geophys. Res.*, 85, 6689-6696.

List of Figures

Figure 1. The model domain with the water column thickness contoured at 50, 100, 500, 1000, 2000, and 3000 m. The Ross Ice Shelf edge is indicated by a dashed line. The locations of tidal elevation observations are indicated by dots and those of velocity observations by triangles.

Figure 2. The amplitude of the M_2 tidal elevation contoured at 1, 2, 5, 10, 15, 20, 25, and 30 cm. The overlaid heavy lines indicate the phase for the elevation, with the zero phase line indicated.

Figure 3. The major axes of the M_2 tidal ellipses for the depth-independent velocities, contoured at 1, 2, 4, 6, 8, 10, and 15 cm s^{-1} .

Figure 4. The major axes of the tidal ellipses from the depth-dependent velocities (dots) compared against those from the observations (triangles) at seventeen mooring locations. The bars indicate the observational uncertainty.

Figure 5. The major axes of the tidal ellipses from the depth-dependent velocities along N-S transects at **a)** $169^\circ 30'$ E, **b)** 176° E, **c)** $179^\circ 30'$ W, **d)** 175° W, and **e)** 160° W. The pairs of letters indicate points discussed in the text (IT-internal tides; RG-reduced generation; VS-vertical shear, 2L- two-layer response). The location of the critical latitude is indicated by a dashed line.

Figure 6. Lead formation estimates from **a)** the depth-dependent surface velocities and **b)** the depth-independent velocities. Contours are shown at 1, 2, 5, 10, and 15 %.

List of Tables

Table 1. Elevation amplitudes and phases from ROMS compared against observational data and other two-dimensional models. Underlined values for the amplitude exceed the observational uncertainty.

Location		Amplitude (cm)				Phase (°)			
Latitude	Longitude	Observations	ROMS	MacAyeal [1984]	Padman [pers. com.]	Observations	ROMS	MacAyeal [1984]	Padman [pers. com.]
84° 15.0' S	171° 19.8' W	8±2	<u>18</u>	<u>16</u>	<u>5</u>	258	273	13	56
82° 31.8' S	166° 0.0' W	8±2	<u>11</u>	7	9	213	202	290	209
82° 22.2' S	168° 37.8' W	7±2	7	<u>4</u>	8	205	202	282	196
81° 11.4' S	170° 30.0' E	3±2	5	<u>6</u>	<u>6</u>	310	21	117	160
80° 11.4' S	161° 33.6' E	5±2	7	<u>15</u>	7	130	27	209	165
79° 45.0' S	169° 3.0' W	3±2	<u>7</u>	<u>8</u>	<u>9</u>	75	95	187	147
79° 31.8' S	163° 38.4' E	4±2	<u>8</u>	<u>8</u>	6	340	36	128	165
79° 15.0' S	170° 19.8' E	3±2	<u>7</u>	<u>7</u>	<u>6</u>	300	49	136	160
78° 12.0' S	162° 16.2' W	3±2	<u>8</u>	<u>9</u>	<u>10</u>	35	72	162	113
77° 51.0' S	166° 39.6' W	4±2	<u>9</u>	<u>8</u>	4	6	57	147	164

Table 1. Elevation amplitudes and phases from ROMS compared against observational data and other two-dimensional models. Underlined values for the amplitude exceed the observational uncertainty.

Figure 1

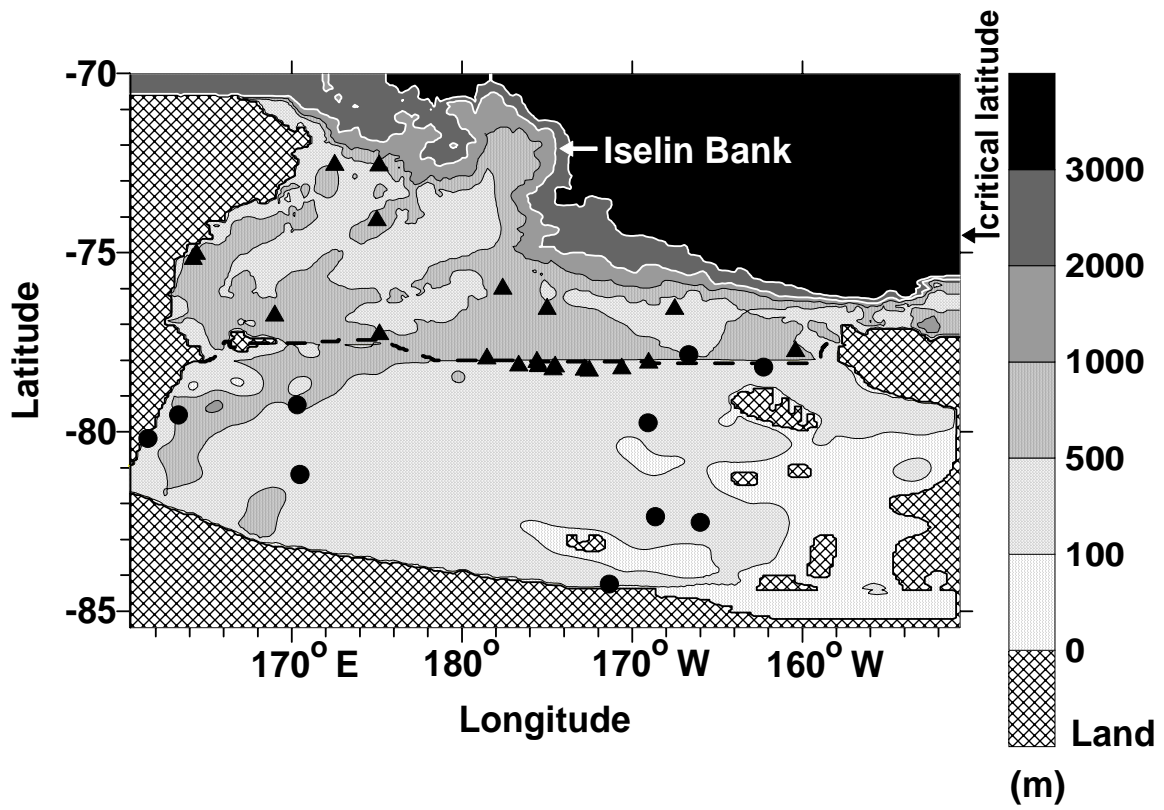


Figure 2

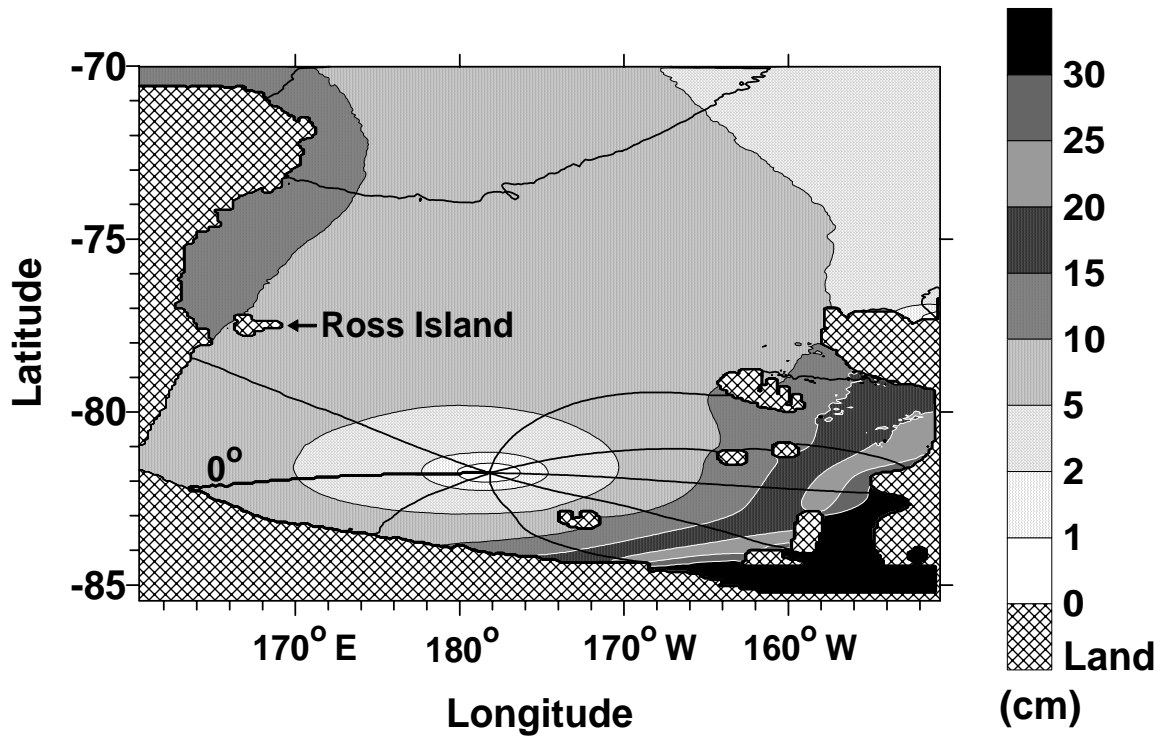


Figure 3

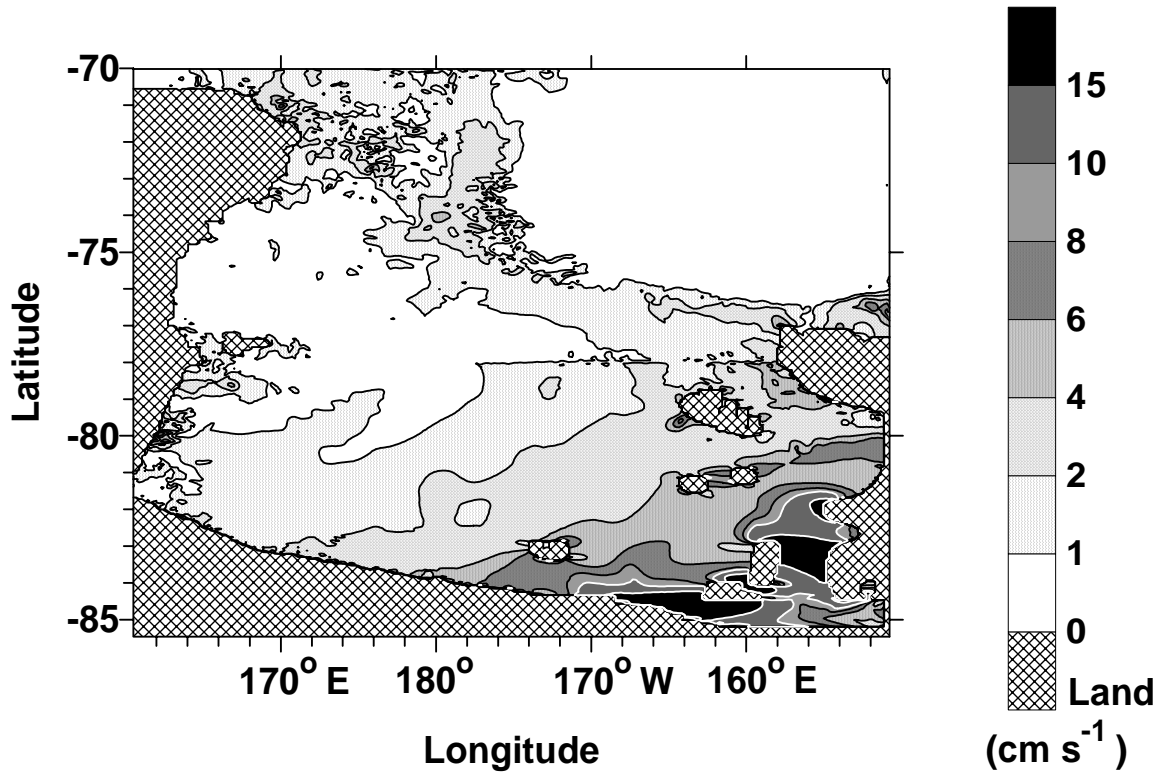


Figure 4

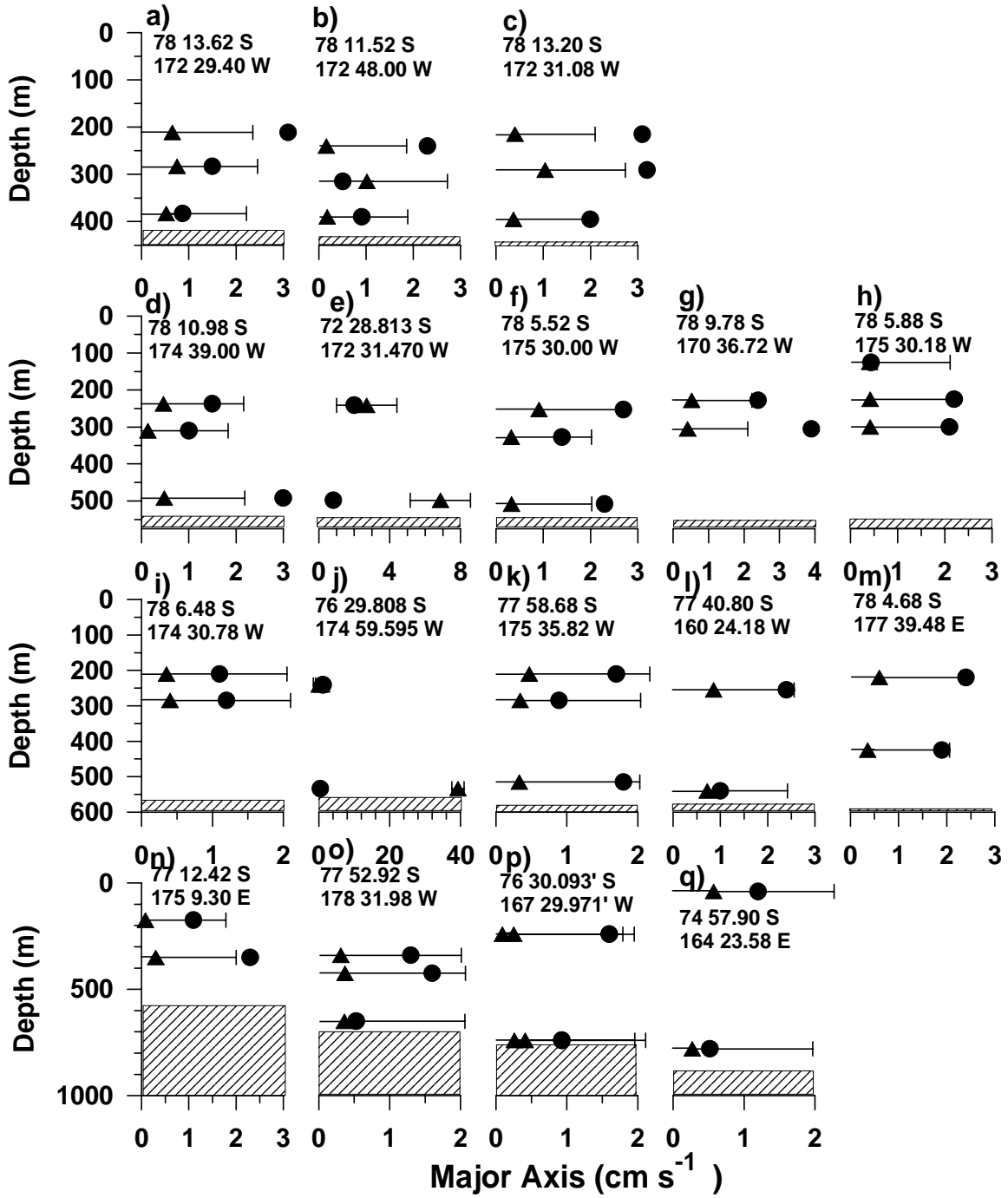


Figure 5

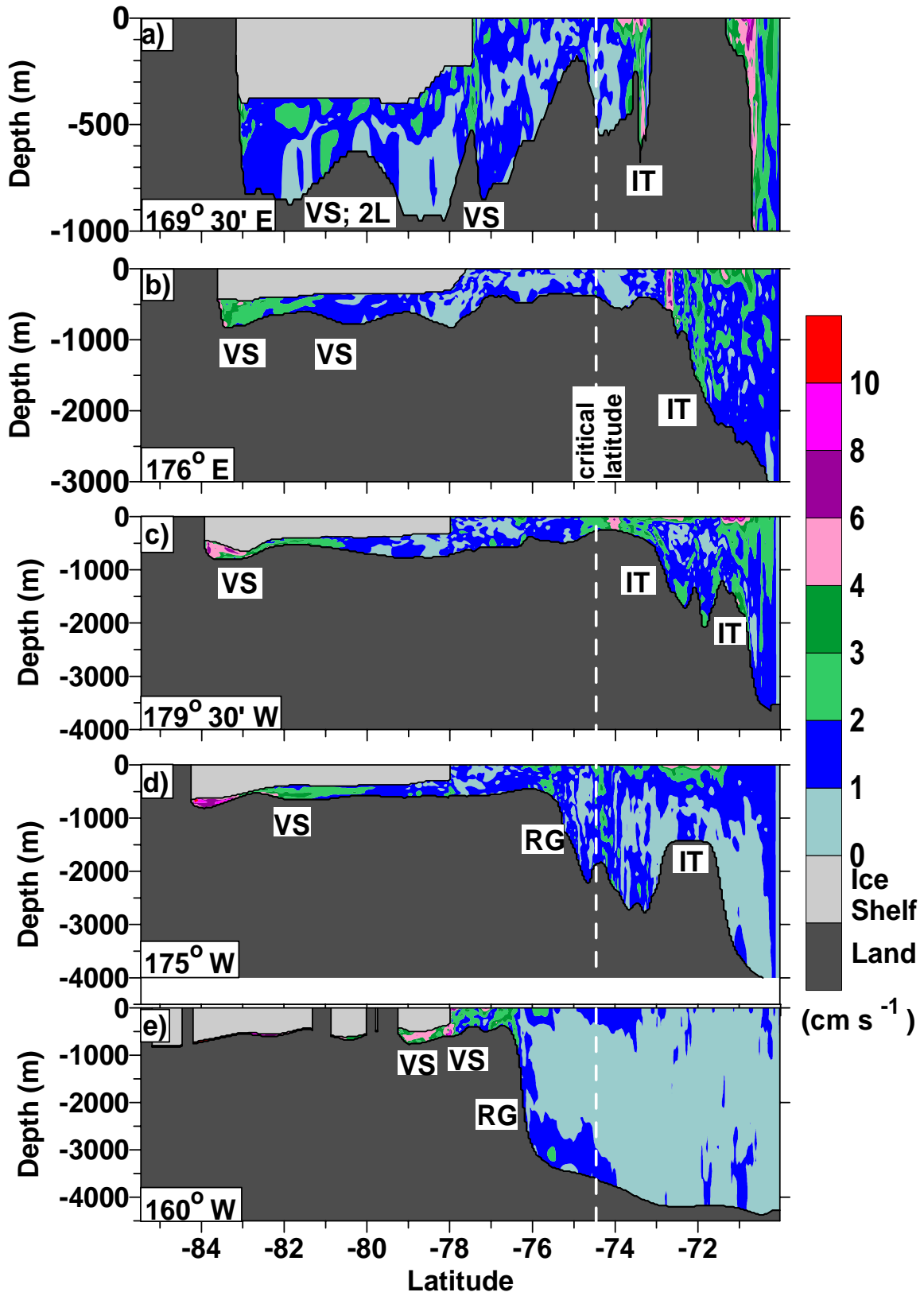


Figure 6

